Focal Mechanism, Magnitude, and Finite-Fault Rapid Estimation Using the Elliptical Patch Method in Chile

by F. Leyton, S. Ruiz, and R. Madariaga

ABSTRACT

Nowadays, most fast, automatic algorithms estimate the magnitude and location of earthquakes assuming a point-source approximation that might produce large errors in the predicted shaking. In this study, using a kinematic approach, we modeled the fault plane as an elliptical patch with a Gaussian slip distribution to perform a rapid estimation of the finite fault, focal mechanism, and moment magnitude. We implemented this finite-fault kinematic inversion using data from the Centro Sismológico Nacional of the Universidad de Chile. We used near-field data, up to 600 km from the epicenter, mostly from accelerograms and a few nonsaturated broadband records. By considering data up to 5 min from the origin time, we are able to retrieve relevant source parameters within 10–15 min from the occurrence of the event. This elliptical patch method (EPM) successfully resolves the source parameters for 45 moderate-to-large events, from 2013 to 2017 (magnitudes ranging from 6.0 to 8.3). These results encourage the use of the EPM in the rapid response to moderate-to-large earthquakes in subduction zones.

Electronic Supplement: Figures showing results of an intermediate depth normal event (11 April 2016 16:20:45 UTC, M_w 6.4) processed with the elliptical patch method (EPM) and tables of models used to compute Green's functions used in this study and model parameters for 45 events.

INTRODUCTION

The rapid characterization of large earthquakes can provide crucial information in the minutes following the event, enabling a preliminary assessment of where the strong ground motion occurred (Wald *et al.*, 1999). Currently, most algorithms attempt to estimate the magnitude and location of the earthquake assuming a point source, such as those used in earthquake early warning (e.g., UrEDAS, Nakamura, 1988, 1989; On-Site, Kanamori, 2005; Earthquake Alarm Systems [ElarmS], Allen and Kanamori, 2003; Virtual Seismologist, Cua and Heaton, 2007). In the near field, the point-source approximation suffers from two drawbacks: it saturates with moderate-to-large magnitudes ($M_w \geq 6.0$) and can overestimate the distance using epicentral distance rather than distance to the fault plane; these factors can severely underestimate the predicted values of the strong ground motions (Böse *et al.*, 2012). Moreover, rapid knowledge of the focal mechanism, fault plane, and the spatial distribution of the slip over the fault should improve the shaking estimation (Dreger *et al.*, 2005), as well as the tsunami forecast (Minson *et al.*, 2014).

After Dreger and Kaverina (2000) proposed a methodology to automatically determine the source process of moderate-magnitude events using a kinematic approach, several researchers attempted to retrieve the fault-plane geometry during the first few minutes after the earthquake using regional data (Ide, 2007 and references therein). Yamada *et al.* (2007) and Yamada and Heaton (2008) extended the methodology by Cua and Heaton (2004) to moderate-to-large earthquakes, where a point-source model can no longer be considered suitable. Recently, Convertito *et al.* (2012) modeled high-frequency data to estimate the surface projection of the rupture plane, along with the dominant rupture direction. Along the same line, the Finite-fault rupture Detector (FinDer) method (Böse *et al.*, 2012, 2015) rapidly estimates a finite source using high-frequency near-source data. Other current methods to estimate fault dimensions focus on Global Navigation Satellite Systems data (GPSlip, Böse *et al.*, 2013; G-larmS, Grapenthin *et al.*, 2014; BEFORES, Minson *et al.*, 2014; G-FAST, Crowell *et al.*, 2016). Many of these methods use a linear inversion approach by fixing the fault plane: either the focal mechanism is known (e.g., Dreger and Kaverina, 2000; Kuge, 2003; Delouis, 2014), or the fault-plane geometry is fixed (Minson *et al.*, 2014).

Here, we use a kinematic approach that simplifies the traditional finite-fault inversion and reduces the computation time: we modeled the fault plane as an elliptical patch with the so-called elliptical patch method (EPM). This methodology uses the long-established discretization of the fault plane into rectangular subfaults (Trifunac, 1974), and makes use of

doi: 10.1785/0220170174

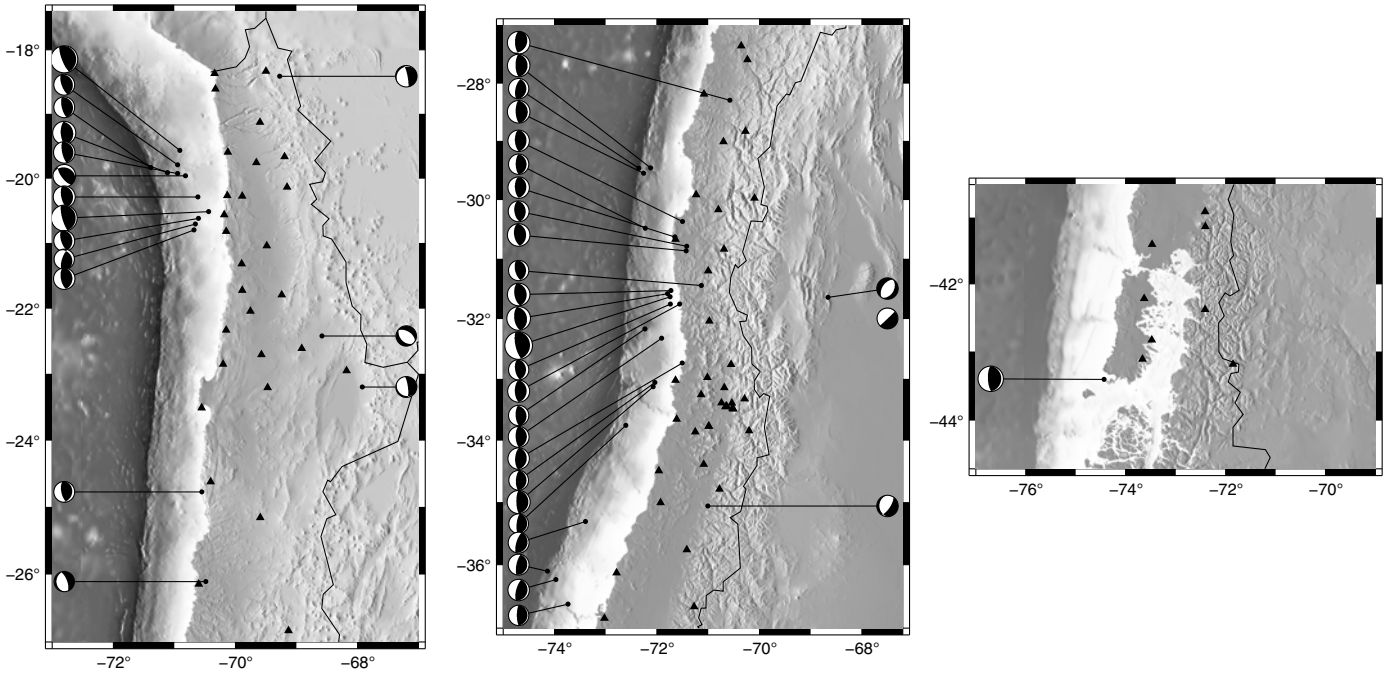

▲ **Figure 1.** Events of magnitude larger than or equal to M_w 6.0 from 2013 to 2017 (circles), their corresponding focal mechanism (reported by the Global Centroid Moment Tensor [CMT]), and the stations used in this study (triangles). Note that the distribution of the stations is not homogenous; see Leyton *et al.* (2018) for details of the Centro Sismológico Nacional (CSN) strong-motion network.

multiple time windows, as in the multi-time-window approach (Olson and Apsel, 1982; Hartzell and Heaton, 1983). However, instead of inverting the source parameters for each subfault, we consider a Gaussian slip distribution over the fault plane, reducing the number of search parameters to less than 10 (Vallée and Bouchon, 2004; Ruiz and Madariaga, 2013; Ulrich and Aochi, 2015; Herrera *et al.*, 2017). This simple source geometry and slip distribution enables us to add other parameters to the inversion, such as the focal mechanism and moment magnitude. We implemented this rapid finite-fault kinematic inversion using data from the Centro Sismológico Nacional (CSN) of the Universidad de Chile and studied the 45 moderate-to-large magnitude events ($6.0 \le M_w \le 8.3$) that occurred between 2013 and 2017 in Chile. In the present work, we begin by describing the data processing, then we introduce the inversion methodology; because of the fact that this corresponds to a nonlinear inversion, we use a stochastic-based method. Afterward, we describe the methodology to automate the inversion, followed by the estimation of seismic moment. Finally, we present the results obtained by applying this methodology to Chilean data, provided by CSN.

METHODOLOGY

We used data recorded between January 2013 and April 2017 for 45 earthquakes recorded at 90 stations that have both strong-motion and broadband seismometers (see Fig. 1). For each event, we limited the analysis to stations less than 600 km from the epicenter. In general, northern and central Chile have denser seismic networks, so more than 10 stations usually record the earthquakes; on the other hand, in southern Chile, fewer stations record the events (Leyton *et al.*, 2018). Strong-motion data were predominantly used; however, broadband recordings were used when it was clear that the traces were not saturated.

Data Processing

In the present study, we considered the hypocenter-determined CSN, obtained from the inversion of body-wave travel times using all available local stations (distances less than 600 km). We fixed the epicentral location (as the point where the rupture starts), allowing changes to the hypocentral depth; locations by CSN sometimes might differ from those of the U.S. Geological Survey, as we will see for the 2016 Chiloé event. All data were processed in the same way:

- We considered 20 s before the theoretical *P*-wave arrival and 180 s after it, resulting in a 200 s time window for all traces, independent of the hypocentral distance.
- Each trace was band-pass filtered, between 0.02 and 0.2 Hz, using a causal two-pole Butterworth filter. The same filters were applied to observed and synthetic traces.
- We removed the instrument response and integrated each trace into displacement, in the time domain.
- Horizontal traces were rotated into radial and transverse components.
- Finally, the data used in the inversion were manually selected by visual inspection of all available records. For the CSN Seismic Network, most of the stations comprise a broadband sensor and an accelerometer, producing six traces for each station (three components from each

sensor). In every case, we considered only one trace per component (radial, transverse, or vertical) for each station, resulting in, at most, three traces per station. The selected traces could be a combination of these two sensors; for example, using the radial and transverse components from the broadband sensor and the vertical component from the accelerometer. In the future, we plan to use an automatic method, based on the signal-to-noise ratio, to select the traces to be used in the inversion.

Inversion Methodology

We implemented the inversion using the neighborhood algorithm (NA), proposed by Sambridge (1999); this method, based on a stochastic Monte-Carlo-based approach, is well suited for nonlinear inverse problems with a small number of parameters. Here, we invert for a set of 10 parameters that completely describe the ellipse's geometry, focal mechanism, and rupture propagation (described in detail in the following paragraph). Using these parameters, we follow the multi-time-window method (Olson and Apsel, 1982; Hartzell and Heaton, 1983) and generate synthetic traces at each of the stations considered. These synthetics are compared with the observed data, defining a fit value that guides the NA's search (see equation 1; Herrmann, 2013).

In the present study, we considered the following 10 parameters to characterize the focal mechanism, magnitude, finite fault, and slip distribution:

- two parameters (a and b) for the semiaxes length (long and short);
- two parameters (Xa and Xb) for the position of the hypocenter inside the ellipse;
- one parameter (α) for the rotation angle of the long semiaxis with respect to the north;
- three parameters (strike, dip, and rake) to define the focal mechanism;
- one parameter (V_r) for the rupture velocity; and
- one parameter (dz) for possible errors in the given depth, ranging from ± 20 km (with respect to the hypocentral depth).

We modified the NA to avoid the previously observed drawback that, sometimes, it might get stuck at local minima. This is implemented by allowing the procedure to explore other solutions, outside the neighborhood of the selected model, by defining a probability of mutation, an approach taken from the genetic algorithm methods. In this case, if a random number exceeds this probability of mutation, the new generated model is not restricted to be inside the Voronoi cell of the selected model. This is repeated for each axis, increasing the region explored in the inversion method. An example is shown in Figure 2 and discussed in detail in the Discussion section.

The synthetic computation was done strictly in a kinematic sense, following the multi-time-window approach (Olson and Apsel, 1982; Hartzell and Heaton, 1983); the rupture starts at the hypocenter and spreads over the elliptical patch with a constant rupture velocity (a model parameter to invert: V_r). Once the rupture front reaches a point, the Green's functions are shifted by the corresponding time delay, combined given the focal mechanism (i.e., strike, dip, and rake), and summed up in the final synthetic; this is repeated for each trace from the data selected. The slip for each subfault is given by the distance to the center of the ellipse, following a Gaussian slip distribution over the ellipse. The ellipse is contained on the plane described by the focal mechanism (strike and dip). We computed the Green's function of each subfault using the Computer Programs in Seismology distribution (Herrmann, 2013) and the CSN 1D regional velocity models presented in Ⓔ Table S1, available in the electronic supplement to this article.

The inversion is done in the time domain, maximizing the fit according to the following cross-correlation criterion

$$\text{fit} = \frac{\sum^{Nt} o(t)p(t)}{\sqrt{\sum^{Nt} o^2(t)p^2(t)}} \tag{1}$$

(Herrmann, 2013), in which $o(t)$ and $p(t)$ are the observed and predicted traces, respectively, and Nt is the total number of traces considered. Using a cross-correlation criterion, the fit is independent of the relative amplitudes; hence, we do not obtain the magnitude during this part of the inversion.

Magnitude Estimation

The magnitude is obtained once all the model parameters are found, defining the best-fitting solution; we performed this estimation in the time and frequency domain. In either domain, we compare the amplitudes of the synthetics and the data and defined the constant K that gives the best fit. In the time domain, we use the following expression to estimate K_t:

$$K_t = \frac{\sum^{Nt} o(t)p(t)}{\sum^{Nt} p^2(t)}. \tag{2}$$

This estimation is done in the previously defined time window (from 20 s before and 180 s after the theoretical P-wave arrival). Conversely, in the frequency domain, the constant K_f is obtained from the average ratio between the observed and the synthetics' Fourier Spectra, in the defined frequency limits (from 0.02 to 0.2 Hz). These constants (K_t and K_f) enable us to estimate the seismic moment, given the units considered in the computations of the Green's functions. From these estimations of the seismic moment, we compute the moment magnitude in the time (M_{w_t}) and frequency (M_{w_f}) domains; this is possible due to the fact that the displacements are linearly dependent with respect to the seismic moment. The resulting magnitudes for each event are presented in Table 1; the difference between these two estimates of M_w is reasonable and similar to the difference with the Global Centroid Moment Tensor (CMT) M_w.

Automatic Inversion Procedure

After several trial-and-errors attempts, we defined the following procedure to perform the inversion:

- we start with 50 initial models (from a random walk on the parameters);

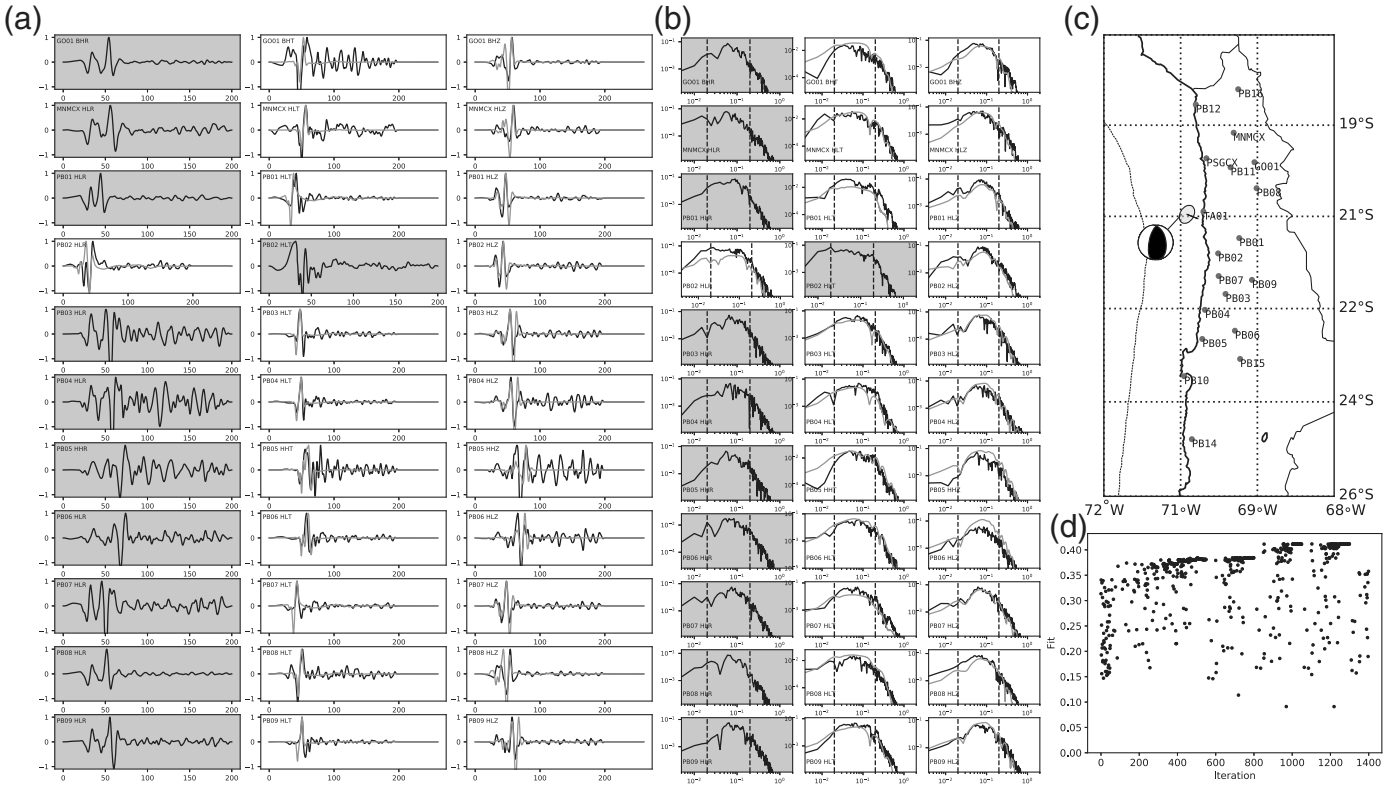

▲ **Figure 2.** Event M_w 6.1 of 4 April 2014, 01:37:52 (UTC). (a) Comparison of synthetic (gray) and observed (black) data in displacement for the best-fitting solution in the time domain. On the upper right corner is shown the station code and component; HN and HL correspond to accelerometers, whereas HH and BH represent broadband sensors. (b) The same comparison of data (black) and the best-fitting solution (gray), but in the frequency domain. For (a,b), highlighted traces in gray were not used in the inversion. (c) Map showing the resulting focal mechanism, the elliptical patch, and the stations used in the inversion. (d) Change of the resulting fit as a function of the model.

- perform 10 iterations, generating 50 new models each cycle (creating 10 new models near the 5 best solutions); and
- afterward, we added cycles of 5 new iterations (with 50 new models each iteration) whenever the fit is increased more than 5% from the previous results.

For the first 10 iterations (and the 50 initial models), we limited the possible ranges of strike, dip, and rake to approximate the usual thrust mechanism observed in the Chilean subduction (i.e., $-10° \le$ strike $\le 10°$; $0° \le$ dip $\le 30°$; $0° \le$ rake $\le 90°$). In the successive iterations, we relaxed this restriction, enabling the program to test all the possible focal mechanisms. However, as can be seen in the data, other focal mechanisms are also resolved by removing this restriction on further iterations. An example can be found in Ⓔ Figure S2, in which an intraplate, intermediate depth, normal event is considered.

Application to CSN

We applied the EPM to all $M_w \ge 6.0$ events in Chile, from 2013 to 2017, a total of 45 events, as shown in Figure 1 and Table 1. The full set of kinematic parameters of these events can be found in Ⓔ Table S2. These events are mostly thrust earthquakes, including the 2014 Iquique (M_w 8.2) and 2015 Illapel (M_w 8.3) earthquakes (Ruiz *et al.*, 2014, 2016), and their corresponding aftershocks (see Fig. 1 and Table 1). In addition, this database also included some intraplate intermediate depth events. As mentioned before, we always first tested the possibility of having a thrust interplate event, setting the focal mechanism accordingly (strike, dip, and rake), releasing this restriction on further iterations. Our results are in agreement with the focal mechanism and magnitude proposed by other agencies: Table 1 shows the Kagan angle (Kagan, 1991) with respect to the best double couple (DC) reported by the Global CMT (Ekström *et al.*, 2012). In the same table are also shown the moment magnitudes reported by the Global CMT and those obtained here, in the time and frequency domain (M_{w_t} and M_{w_f}, respectively) and estimations of the half-duration (HD, in Table 1); our estimations of the HD present errors, on average, of less than of 20% with respect to those of the Global CMT.

An example is shown in Figure 2, for a magnitude M_w 6.1 event (4 April 2014, 01:37:52 UTC), an aftershock of the 2014 Iquique earthquake. This event corresponds to an interplate thrust earthquake (Ruiz *et al.*, 2014); details can be found in the figure caption. Panel (d) shows that the fit does not systematically improve with each iteration; this is due to the random mutation added to NA, as discussed in the Inversion Methodology section.

Table 1
Events Studied in This Work Identified by Global CMT code

Event	Global CMT M_w	EPM M_{w_t}	EPM M_{w_f}	Global CMT HD (s)	EPM HD (s)	Ka with Respect to Global CMT	Percentage DC
201301302015A	6.8	6.4	6.4	6.0	4.9	22.9	96.1
201310300251A	6.3	6.3	6.3	3.3	4.1	16.2	93.6
201310312303A	6.5	6.2	6.4	4.3	4.8	21.6	95.6
201403162116A	6.7	6.6	6.7	5.3	6.2	41.9	58.0
201403170511A	6.4	6.4	6.8	3.8	4.2	30.3	93.5
201403221259A	6.3	6.2	6.3	3.2	4.3	31.1	91.1
201403231819A	6.3	6.2	6.4	3.2	4.2	32.7	92.9
201404012346A	8.2	7.9	8.1	28.0	23.8	37.8	98.7
201404012358A	7.0	6.8	6.9	7.7	9.5	20.7	91.6
201404030158A	6.6	6.4	6.6	4.8	6.2	15.8	89.4
201404030243A	7.8	7.0	7.5	17.9	15.6	32.5	97.7
201404030526A	6.5	6.3	6.2	4.3	3.9	25.7	78.4
201404040137A	6.3	6.1	6.1	3.2	3.3	34.8	95.6
201404110001A	6.1	6.1	6.1	2.7	3.2	11.3	84.2
201408232232A	6.5	6.1	6.3	4.0	4.1	11.6	89.8
201502021049A	6.3	6.1	6.2	3.3	3.0	19.1	15.4
201503181827A	6.2	6.3	6.5	2.8	3.4	8.7	91.4
201503230451A	6.5	6.6	6.8	4.0	4.6	18.2	89.2
201506101352A	6.1	6.4	6.4	2.6	3.2	7.4	81.1
201506200210A	6.4	6.5	6.5	3.9	5.2	14.3	93.8
201509162254A	8.3	7.5	7.7	33.4	21.3	33.4	95.0
201509162318A	7.1	6.8	7.0	8.7	8.2	15.9	84.1
201509170410A	6.8	6.5	6.5	5.9	4.6	21.8	78.0
201509180910A	6.1	6.2	6.2	2.7	3.2	4.4	95.2
201509191252A	6.3	6.0	6.2	3.1	3.9	23.3	96.5
201509210539A	6.1	5.9	6.0	2.7	3.4	21.8	94.6
201509211739A	6.6	6.3	6.5	4.8	5.9	50.6	96.9
201509220712A	6.1	6.1	6.3	2.6	3.1	24.8	83.6
201509260251A	6.3	6.1	6.8	3.3	4.0	28.3	85.1
201511070704A	6.1	6.1	6.3	2.6	3.5	36.5	99.4
201511070731A	6.7	6.6	6.8	5.5	6.0	25.4	90.5
201511110154A	6.8	6.6	7.1	6.1	7.8	14.5	99.3
201511110246A	6.8	6.7	6.9	6.1	7.6	7.8	97.8
201511272100A	6.2	5.9	5.8	3.0	2.9	19.1	89.2
201602100033A	6.4	6.2	6.4	3.7	4.8	29.8	95.9
201602220637A	6.1	5.8	6.0	2.5	3.5	9.1	96.7
201607251726A	6.1	6.1	6.3	2.6	3.5	15.4	33.1
201610272032A	6.0	6.0	5.9	2.4	2.6	10.8	97.1
201611041620A	6.4	6.6	6.7	3.5	3.8	14.3	80.5
201611080455A	6.1	6.0	6.1	2.4	2.5	21.1	95.5
201611202057A	6.4	6.5	6.5	3.9	3.7	19.0	54.9

Events studied in this work are identified by their corresponding Global Centroid Moment Tensor (CMT) code and the different moment magnitudes considered in this study: reported by the Global CMT, obtained in this study, using the elliptical patch method (EPM) in the time domain (EPM M_{w_t}) and the frequency domain (EPM M_{w_f}), the half-duration (HD) reported by the Global CMT and this study (EPM), the Kagan angle with respect to the best double-couple (DC) focal mechanism reported by the Global CMT, and the percentage of DC from the Global CMT focal mechanism.
(Continued next page.)

Table 1 (continued)
Events Studied in This Work Identified by Global CMT code

Event	Global CMT M_w	EPM M_{w_t}	EPM M_{w_f}	Global CMT HD (s)	EPM HD (s)	Ka with Respect to Global CMT	Percentage DC
201612251422A	7.6	7.3	7.7	14.9	11.8	21.2	98.7
201704150819A	6.3	6.2	6.4	3.3	3.9	22.3	55.3
201704230236A	6.0	5.9	6.1	2.4	2.5	18.3	97.1
201704242138A	6.9	6.7	6.9	6.1	6.4	14.9	98.2

Events studied in this work are identified by their corresponding Global Centroid Moment Tensor (CMT) code and the different moment magnitudes considered in this study: reported by the Global CMT, obtained in this study, using the elliptical patch method (EPM) in the time domain (EPM M_{w_t}) and the frequency domain (EPM M_{w_f}), the half-duration (HD) reported by the Global CMT and this study (EPM), the Kagan angle with respect to the best double-couple (DC) focal mechanism reported by the Global CMT, and the percentage of DC from the Global CMT focal mechanism.

Figure 3 shows a comparison of the moment magnitude estimated in this study (M_w EPM) with respect those published by CMT (M_w Global CMT). From this figure, we see that, for most cases, there is a good agreement between our results and CMT, except for a megathrust event, 2015 Illapel (M_w 8.3). Our method obtained a magnitude of M_w 7.7; this could be due to the short time window considered (only 5 min after the origin time), the restricting frequency band (from 0.02 to 0.2 Hz), or the complex seismic rupture (Ruiz *et al.*, 2016). This aspect should be further explored in future works.

All the results presented in this study were computed using traces cut 5 min after the origin time, enabling the clear recording of the *S* waves up to 600 km. Nevertheless, we tested a time window of 2 min after the origin time and were able to successfully retrieve most of the parameters (see Ⓔ Figs. S1, S3, and S5); for these cases, the maximum hypocentral distance to the considered stations was reduced from 600 to 300 km. For this decrease in the time window to successfully work, the most important requirement is the availability of good-quality data. From Figure 1 and Ⓔ Figure S2, we observe that northern and central Chile have a sufficiently dense network that enables the use of short time windows; these cases used a 5-min time window after the origin time. For these events, the results are comparable using only a 2-min time window after origin time, as shown in Ⓔ Figures S1 and S3. On the other hand, regions with sparse networks, such as southern Chile, require longer time windows to get a reasonable amount of good-quality data. An example considering 5- and 2-min time windows is presented in Ⓔ Figures S4 and S5, respectively. We found that, for the 2-min time window, only two stations were able to successfully record the event; whereas for the 5-min time window, a large number of stations became available, enabling a better estimation of the source parameters. Hence, the possibility of reducing the time window after origin time strongly depends on the geometry of the network; however, an automatic method considering different time windows after the origin time could be explored, as was done by Ulrich and Aochi (2015).

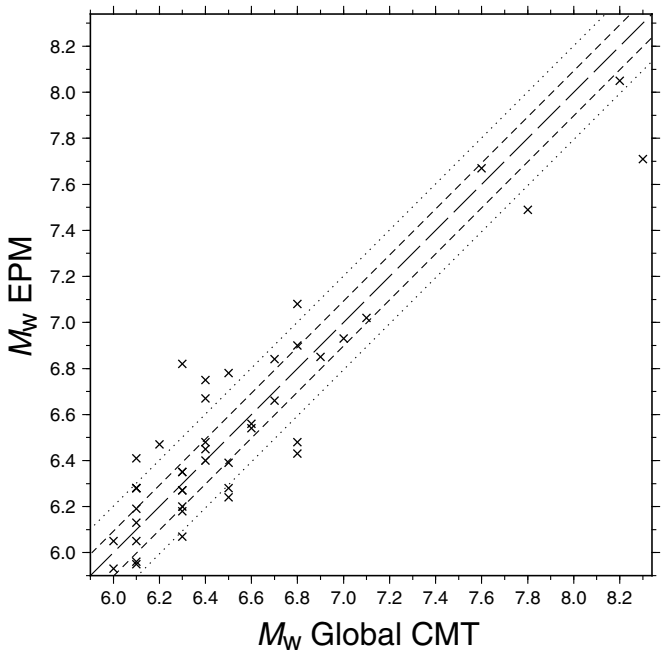

▲ **Figure 3.** Comparison of moment magnitudes reported by the Global CMT and those obtained here (estimated in the frequency domain: M_{w_f}); the long dashed lines show the exactly equal values, and short dashed and dotted lines show the difference from the equal values ±0.1 and ±0.2, respectively.

We found that the focal mechanism, fault plane, and magnitude are robustly estimated, being able to constrain them in a few iterations. Figure 4 shows a comparison of the slip distribution obtained in this study with results available from Hayes (2017), taken from the earthquake pages of the National Earthquake Information Center's (NEIC) Combined Catalog (see Data and Resources). In general, there is a good agreement between both results, except for the 2016 Chiloé earthquake (panel d). This difference is due to the shift between the epicenters determined by NEIC and CSN (shown in red and blue stars in Fig. 4, respectively) and the fact that both procedures constrain the fault-plane solution to contain the hypocenter. Some important differences are also shown for the 2017

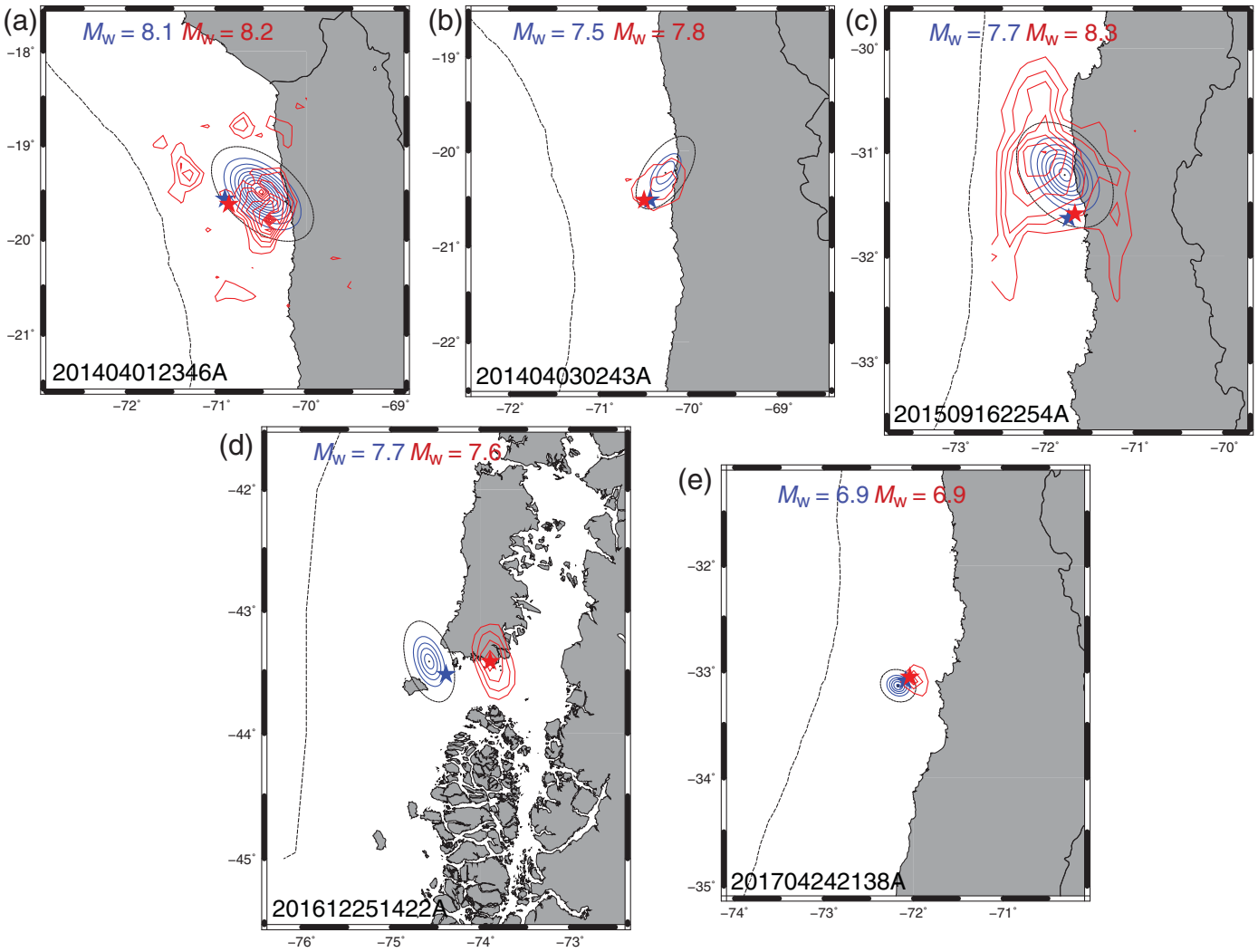

▲ **Figure 4.** Comparison of the slip distribution determined by this study and those of Hayes (2017), shown with blue and red contour lines, respectively. Contour lines are plotted every 1 m in both cases, except for (e) that are plotted every 20 cm; stars represent the epicenter reported by the National Earthquake Information Center and the CSN, in red and blue, respectively. Panels presents the following events: (a) 2014 Iquique, (b) largest aftershock of the 2014 Iquique earthquake, (c) 2015 Illapel, (d) 2016 Chiloé, and (e) 2017 Valparaíso. At the top of each panel is shown the corresponding moment magnitude, in red reported by the Global CMT and in blue the one obtained in this study; at the bottom is shown its Global CMT code, for reference.

Valparaíso event (panel e), in which NEIC's solution places the main slip toward the east of the hypocenter, whereas our results locate the slip toward the West.

The rupture velocity and dimensions of the fault plane are more difficult to resolve. To improve these estimations, we performed a second inversion fixing the focal mechanism, focusing the inversion in the parameters describing the geometry of the fault plane. We further restricted the inversion by limiting the space parameter to reasonable values, allowing for a 50% variation around the estimated parameters, using the empirical relations defined by Papazachos *et al.* (2004). This secondary inversion shows a remarkable improvement of the estimations of the fault-plane geometry, as shown in Figure 5, but no significant changes for the rupture velocity (V_r) were observed. We believe that the EPM lacks resolution of V_r, as shown in Ⓔ Figure S6, resulting only in broad ranges for this parameter, from 2.6 to 2.8 km/s for interplate thrust events and from 2.8 to 3.2 km/s for intraplate intermediate depth events, with a few exceptions (see figure captions for details). Hence, we propose that this parameter should be fixed in the inversion.

DISCUSSION

The present study presents a rapid methodology to obtain relevant source parameters such as focal mechanism, moment magnitude, and a first-order estimation of the finite-fault surface using the EPM. All the available near-filed data are used, mostly accelerograms and a few nonsaturated broadbands. This method has been successfully tested for moderate-to-large magnitude earthquakes ($6.0 \leq M_w \leq 8.3$) recorded by the CSN seismic network, with the exception of the megathrust 2015 Illapel event (M_w 8.3). This could be due to source complex-

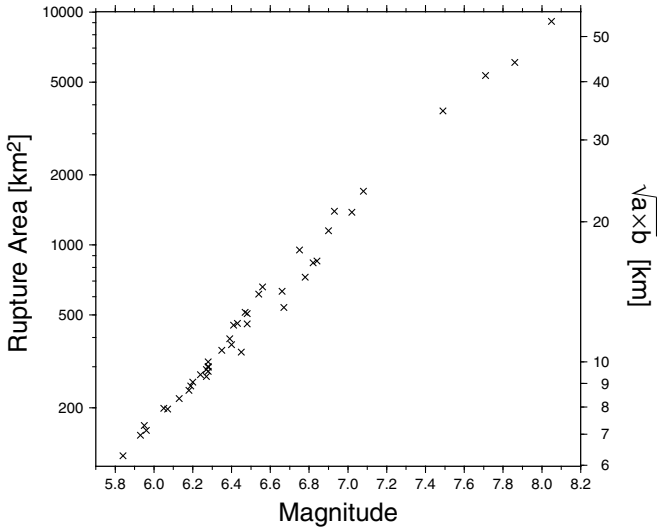

▲ **Figure 5.** Rupture area as a function of the moment magnitude estimated in this study, for each event considered. We also show, in the right vertical axis, the characteristic dimension, computed as the geometrical average of the ellipse's semiaxes (a,b).

ities that do not allow for a single ellipse to be used, requiring more than one large slip patch.

We proposed a modified NA to perform the nonlinear inversion. We took advantage of the fact that, for each iteration, the space parameter can be easily modified, focusing the search in models' subspaces that are in agreement with the tectonic environment. For example, the first iterations are restricted to plausible thrust focal mechanism, most commonly observed in the Chilean subduction environment. The restriction of the model parameters does not influence the cost function; hence, a second run done after enlarging this space parameter can be done given the previously computed models. In a similar way, the geometry of the fault plane can be better estimated by a second inversion, restricting the space parameter that defines the focal mechanism.

We found several cases in which the Kagan angle (Ka) of the obtained focal mechanism differed from the one reported by the Global CMT by as much as 30°. After a detailed examination, we found that these cases corresponds to large amplitude events ($M_w \geq 7.8$) or cases in which the network did not give a good azimuthal coverage, having most of the stations located either to the south or to the north of the epicenter. In only one case, we found that the large Ka = 41.9° could be produced by a small DC percentage from the Global CMT's focal mechanism (event 201310312303A in Table 1). On the other hand, magnitude estimations by EPM seem to be underestimated for large events ($M_w \geq 7.8$); this could be due to the limitation of the use of a 5-min time window after the origin time.

The results presented here considered a time window of 5 min after the origin time, but a 2-min time window was also tested, with varying results, depending on the geometry of the network. We believe that an automatic procedure should consider different time windows, running in parallel, to better constraint the source parameters. To address this issue, we are currently exploring the possibility of parallelizing the code in a cluster, to reduce its computation time and enable a real-time implementation at the CSN. Nevertheless, we conclude that the actual EPM version enables a rapid and robust estimation of the source parameters for moderate-to-large earthquakes in Chile, using near-field data.

DATA AND RESOURCES

All records used here were provided by the Centro Sismológico Nacional (CSN) of the Universidad de Chile, most of them retrieved from the Strong-motion Data Base (evtdb.csn.uchile.cl, last accessed June 2017). Combined Catalog (ComCat) data were obtained from http://earthquake.usgs.gov/earthquakes/map/ (last accessed December 2017).

ACKNOWLEDGMENTS

Some routines used in this study were taken from Computer Programs in Seismology (Herrmann, 2013). Revisions made by Associate Editor B. Crowell and an anonymous reviewer were very helpful in improving this article. Figures were made using Generic Mapping Tools (GMT) software (Wessel and Smith, 1998). The authors acknowledge the support from Programa de Riesgo Sísmico (AIN, University of Chile) and of Fondecyt projects N° 1170218 and 1170430.

REFERENCES

Allen, R. M., and H. Kanamori (2003). The potential for earthquake early warning in southern California, *Science* **300,** no. 5620, 786–789.

Böse, M., C. Felizardo, and T. H. Heaton (2015). Finite-fault rupture detector (FinDer): Going real-time in Californian ShakeAlert warning system, *Seismol. Res. Lett.* **86,** no. 6, doi: 10.1785/0220150154.

Böse, M., T. H. Heaton, and E. Hauksson (2012). Real-time finite fault rupture detector (FinDer) for large earthquakes, *Geophys. J. Int.* **191,** no. 2, 803–812.

Böse, M., T. H. Heaton, and K. W. Hudnut (2013). Combining real-time seismic and GPS data for earthquake early warning, *AGU Fall Meeting Abstracts*, Abstract ID G51B–05.

Convertito, V., N. Maercklin, N. Sharma, and A. Zollo (2012). From induced seismicity to direct time-dependent seismic hazard, *Bull. Seismol. Soc. Am.* **102,** no. 6, 2563–2573.

Crowell, B. W., D. A. Schmidt, P. Bodin, J. E. Vidale, J. Gomberg, J. R. Hartog, V. C. Kress, T. I. Melbourne, M. Santillan, S. E. Minson, *et al.* (2016). Demonstration of the Cascadia G-FAST geodetic earthquake early warning system for the Nisqually, Washington, earthquake, *Seismol. Res. Lett.* **87,** no. 4, doi: 10.1785/0220150255.

Cua, G., and T. Heaton (2004). Characterizing average properties of southern California ground motion envelopes, *2004 SCEC Annual Meeting Proceedings and Abstracts*, Vol. 14, 10.

Cua, G., and T. Heaton (2007). The Virtual Seismologist (VS) method: A Bayesian approach to earthquake early warning, in *Earthquake Early Warning Systems*, Springer, Berlin, Heidelberg, 97–132.

Delouis, B. (2014). FMNEAR: Determination of focal mechanism and first estimate of rupture directivity using near-source records and a linear distribution of point sources, *Bull. Seismol. Soc. Am.* **104,** no. 3, 1479–1500, doi: 10.1785/0120130151.

Dreger, D., and A. Kaverina (2000). Seismic remote sensing for the earthquake source process and near-source strong shaking: A case study

of the October 16, 1999 Hector Mine earthquake, *Geophys. Res. Lett.* **27,** no. 13, 1941–1944.
Dreger, D. S., L. Gee, P. Lombard, M. H. Murray, and B. Romanowicz (2005). Rapid finite-source analysis and near-fault strong ground motions: Application to the 2003 M_w 6.5 San Simeon and 2004 M_w 6.0 Parkfield earthquakes, *Seismol. Res. Lett.* **76,** no. 1, 40–48.
Ekström, G., M. Nettles, and A. M. Dziewonski (2012). The global CMT project 2004-2010: Centroid-moment tensors for 13,017 earthquakes, *Phys. Earth Planet. In.* **200/201,** 1–9, doi: 10.1016/j.pepi.2012.04.002.
Grapenthin, R., I. A. Johanson, and R. M. Allen (2014). Operational real-time GPS-enhanced earthquake early warning, *J. Geophys. Res.* **119,** no. 10, 7944–7965.
Hartzell, S. H., and T. H. Heaton (1983). Inversion of strong ground motion and teleseismic waveform data for the fault rupture history of the 1979 Imperial Valley, California, earthquake, *Bull. Seismol. Soc. Am.* **73,** 1553–1583.
Hayes, G. P. (2017). The finite, kinematic rupture properties of great-sized earthquakes since 1990, *Earth Planet. Sci. Lett.* **468,** 94–100.
Herrera, C., S. Ruiz, R. Madariaga, and P. Poli (2017). Dynamic inversion of the 2015 Jujuy intermediate depth and similarity with other intraslab events, *Geophys. J. Int.* **209,** no. 2, 866–875, doi: 10.1093/gji/ggx056.
Herrmann, R. B. (2013). Computer programs in seismology: An evolving tool for instruction and research, *Seismol. Res. Lett.* **84,** 1081–1088, doi: 10.1785/0220110096.
Ide, S. (2007). Slip inversion, in *Earthquake Seismology*, H. Kanamori (Editor), Treatise on Geophysics, Vol. 4. Elsevier, Amsterdam, The Netherlands, 193–224.
Kagan, Y. Y. (1991). 3-D rotation of double-couple earthquake sources, *Geophys. J. Int.* **106,** 709–716.
Kanamori, H. (2005). Real-time seismology and earthquake damage mitigation, *Annu. Rev. Earth Planet. Sci.* **33,** 195–214.
Kuge, K. (2003). Source modeling using strong-motion waveforms: Toward automated determination of earthquake fault planes and moment-release distributions, *Bull. Seismol. Soc. Am.* **93,** 639–654.
Leyton, F., C. Pastén, S. Ruiz, B. Idini, and F. Rojas (2018). Empirical site classification of CSN network using strong-motion records, *Seismol. Res. Lett.* **89,** no. 2A, doi: 10.1785/0220170167.
Minson, S. E., J. R. Murray, J. O. Langbein, and J. S. Gomberg (2014). Real-time inversions for finite fault slip models and rupture geometry based on high-rate GPS data, *J. Geophys. Res.* **119,** 3201–3231.
Nakamura, Y. (1988). On the urgent earthquake detection and alarm system (UrEDAS), *Proc. of the 9th World Conf. on Earthquake Engineering*, Vol. 7, 673–678.
Nakamura, Y. (1989). A method for dynamic characteristics estimation of subsurface using microtremor on the ground surface, *Q. Rep. Railway Tech. Res. Inst.* **30,** no. 1, 25–33.
Olson, A. H., and R. J. Apsel (1982). Finite faults and inverse theory with applications to the 1979 Imperial Valley earthquake, *Bull. Seismol. Soc. Am.* **72,** 1969–2001.
Papazachos, B. C., E. M. Scordilis, D. G. Panagiotopoulos, C. B. Papazachos, and G. F. Karakaisis (2004). Global relations between seismic fault parameters and moment magnitude of earthquakes, *Bull. Geol. Soc. Greece* **36,** no. 3, 1482–1489.
Ruiz, S., and R. Madariaga (2013). Kinematic and dynamic inversion of the 2008 Northern Iwate earthquake, *Bull. Seismol. Soc. Am.* **103,** 694–708.
Ruiz, S., E. Klein, F. del Campo, E. Rivera, P. Poli, M. Metois, V. Christophe, J. C. Baez, G. Vargas, F. Leyton, *et al.* (2016). The seismic sequence of the 16 September 2015 M_w 8.3 Illapel, Chile, earthquake, *Seismol. Res. Lett.* **87,** no. 4, doi: 10.1785/0220150281.
Ruiz, S., M. Metois, A. Fuenzalida, J. Ruiz, F. Leyton, R. Grandin, C. Vigny, R. Madariaga, and J. Campos (2014). Intense foreshocks and a slow slip event preceded the 2014 Iquique M_w 8.1 earthquake, *Science* **345,** no. 6201, 1165–1169.
Sambridge, M. (1999). Geophysical inversion with a neighborhood algorithm—I. Searching a parameter space, *Geophys. J. Int.* **138,** 479–494.
Trifunac, M. D. (1974). A three-dimensional dislocation model for the San Fernando, California, earthquake of February 9, 1971, *Bull. Seismol. Soc. Am.* **64,** no. 1, 149–172.
Ulrich, T., and H. Aochi (2015). Rapidness and robustness of finite-source inversion of the 2011 M_w 9.0 Tohoku earthquake by an elliptical-patches method using continuous GPS and acceleration data, *Pure Appl. Geophys.* **172,** no. 12, 3439–3453.
Vallée, M., and M. Bouchon (2004). Imaging coseismic rupture in far field by slip patches, *Geophys. J. Int.* **156,** 615–630.
Wald, D. J., V. Quitoriano, T. H. Heaton, H. Kanamori, C. W Scrivner, and C. B. Worden (1999). TriNet ShakeMaps: Rapid generation of instrumental ground motion and intensity maps for earthquakes in southern California, *Earthq. Spectra* **15,** 537–555.
Wessel, P., and W. H. F. Smith (1998). New improved version of generic mapping tools released, *Eos Trans. AGU* **79,** 579.
Yamada, M., and T. Heaton (2008). Real-time estimation of fault rupture extent using envelopes of acceleration, *Bull. Seismol. Soc. Am.* **98,** no. 2, 607–619.
Yamada, M., T. Heaton, and J. Beck (2007). Real-time estimation of fault rupture extent using near-source versus far-source classification, *Bull. Seismol. Soc. Am.* **97,** no. 6, 1890–1910.

F. Leyton
Centro Sismológico Nacional
Universidad de Chile
Blanco Encalada 2002
Santiago 8370449, Chile
leyton@csn.uchile.cl

S. Ruiz
Dept. Geofísica
Universidad de Chile
Blanco Encalada 2002
Santiago 8370449, Chile

R. Madariaga
Laboratoire de Géologie
Ecole Normale Supérieure
24 rue Lhomond
75231 Paris, cedex 05
France

Published Online 14 February 2018